

Article

# Anion Intercalation/De-Intercalation Mechanism Enabling High Energy and Power Densities of Lithium-Ion Capacitors

Yang Zhang , Junquan Lao  and Ping Xiao  \*

Department of Materials, Henry Royce Institute, University of Manchester, Manchester M13 9PL, UK;  
yang.zhang-26@postgrad.manchester.ac.uk (Y.Z.); junquan.lao@manchester.ac.uk (J.L.)

\* Correspondence: p.xiao@manchester.ac.uk

**Abstract:** The growing demands for electrochemical energy storage systems is driving the exploration of novel devices, with lithium-ion capacitors (LICs) emerging as a promising strategy to achieve both high energy density and fast charge capability. However, the low capacitance of commercial activated carbon (AC) cathode based on anion absorption/desorption limits LIC applications. Herein, commercial graphite is proposed as the cathode to construct an innovative AC (−)/graphite (+) system. The graphite cathode functions as anion hosting, allowing reversible intercalation/de-intercalation of anions into/from its interlayers. The as-designed AC (−)/graphite (+) full cell achieves stable cycling with 90.6% capacity retention after 200 cycles at  $0.1 \text{ A g}^{-1}$  and a prolonged lifespan with 87.5% capacity retention after 5000 cycles at  $0.5 \text{ A g}^{-1}$  with the upper cut-off voltage of 5.0 V, yielding a high average Coulombic efficiency (CE) of 99.3%. Moreover, the full cell exhibits a high energy density ( $>200 \text{ Wh kg}^{-1}$ ) and power density of  $7.7 \text{ kW kg}^{-1}$  (calculated based on active mass in both electrodes). These performances exceed most LICs based on anions absorption/desorption on the surface of AC cathodes. This work explores an effective electrode revolution with the assistance of anion intercalation/de-intercalation chemistry for developing novel LICs with high energy and power densities.

**Keywords:** lithium-ion capacitor; hybrid dual-ion system; graphite cathode; anion intercalation/de-intercalation; energy density



**Citation:** Zhang, Y.; Lao, J.; Xiao, P. Anion Intercalation/De-Intercalation Mechanism Enabling High Energy and Power Densities of Lithium-Ion Capacitors. *Batteries* **2024**, *10*, 296. <https://doi.org/10.3390/batteries10090296>

Academic Editor: Johan E. ten Elshof

Received: 23 July 2024

Revised: 13 August 2024

Accepted: 21 August 2024

Published: 23 August 2024



**Copyright:** © 2024 by the authors. Licensee MDPI, Basel, Switzerland. This article is an open access article distributed under the terms and conditions of the Creative Commons Attribution (CC BY) license (<https://creativecommons.org/licenses/by/4.0/>).

## 1. Introduction

Addressing the increasing global energy demands requires advancements in electrochemical devices, given their wide-ranging applications from portable electronics to electric transportation to the integration of renewable energy sources for powering the electrical grid [1,2]. Lithium-ion batteries (LIBs) have emerged as the predominant energy storage and conversion device owing to its high energy density ( $>300 \text{ Wh kg}^{-1}$ ), yet the lower power density remains a notable challenge [3,4]. In comparison to extensively researched LIBs, supercapacitors (electrical double-layer capacitors) typically consist of a symmetrical structure composed of high surface area carbon materials such as activated carbon (AC). This configuration facilitates rapid energy storage through ion adsorption/desorption on the surface of the AC, consequently achieving high power density and a long cycling life, but their practical application is limited by lower energy density ( $<10 \text{ Wh kg}^{-1}$ ) [5]. Therefore, there is a strong appeal for innovative electrochemical energy storage and conversion devices that integrate the merits of both batteries (high energy density) and supercapacitors (high power density).

Lithium-ion capacitors (LICs), utilising a battery-type anode (graphite or  $\text{Li}_4\text{Ti}_5\text{O}_{12}$ ) driven by Faraday reactions (mainly intercalation/deintercalation behaviour) and a capacitor-type cathode operating on non-Faraday reactions (absorption/desorption behaviour), have been developed to achieve enhanced energy density ( $20\text{--}146 \text{ Wh kg}^{-1}$ ) [6]. However, the energy density of commercial AC cathode-based LICs via anion absorption/desorption behaviour

during charging/discharging processes is constrained by the limitation of low capacitance and low stable working voltage (<4.6 V versus Li/Li<sup>+</sup>) [7–9]. Building upon this foundation, considerable efforts have been made, encompassing the exploration of high-capacitance electrode materials, surpassing commercial AC to construct high-voltage devices [10,11].

Graphite, consisting of stacked layers of graphene held together by weak van der Waals force, has the capability to electrochemically accommodate charge carriers. The graphite can form acceptor-type graphite interphase compounds (GICs) by stabilising additional holes in its bonding π-band, allowing for the intercalation/de-intercalation of anions. Typically, the charge-transfer reaction with the intercalation/de-intercalation of anions is exhibited as Equation (1) [12].



The graphite cathode demonstrates favourable operation at a high upper cut-off voltage of 5.3 V, yielding a medium voltage of around 4.6 V, which is significant compared to most cathode materials. The high working voltage ensures a potentially high energy density. Typically, graphite cathode is coupled with graphite anode to construct dual-graphite batteries. However, the dual-graphite batteries face challenges, including a limited rate capability and, particularly, a short cycle life. These issues are primarily due to the insufficient reaction kinetics of the graphite anode, which experiences inevitable capacity decay with increasing the current density up to 300 mA g<sup>-1</sup> [13]. In contrast, the graphite cathode is expected to exhibit superior rate performance, capable of sustaining a stable capacity close to its theoretical value of approximately 100 mAh g<sup>-1</sup> even at a high current density up to 2 A g<sup>-1</sup> [14]. Remarkably, the high operating voltage and excellent rate performance of the graphite cathode contribute to maximising the advantages of LICs incorporating an AC anode, especially in terms of rapid and stable charge storage. This suggests promising potential for developing innovative high-energy and high-power LICs based on anion intercalation chemistry. However, this novel construction is still in the early stages of research, with limited studies primarily focusing on the low voltage range (0–4.5 V), demonstrating low energy density (<100 Wh kg<sup>-1</sup>) [15–17]. Therefore, optimising and matching the graphite cathode and electrolyte to unlock performance at higher voltages and achieve a prolonged cyclic life is of great significance. Furthermore, there is substantial room for improvement in the fundamental and technical principles of this system, as well as in the exploration of its working mechanisms.

Herein, we propose the construction of novel LICs featuring an AC anode and graphite cathode in a standard concentration electrolyte (1M LiPF<sub>6</sub> EMC), employing the combination of cation absorption/desorption and anion intercalation/de-intercalation chemistry. The as-prepared AC (−)/graphite (+) full cell is operated at a high voltage range of 2.0–5.0 V, with a medium voltage above 4.2 V at the current density of 0.1 A g<sup>-1</sup>. As expected, excellent cyclic stability (90.6% capacity retention after 200 cycles at 0.1 A g<sup>-1</sup>) and long-term cycle life (87.5% capacity retention after 5000 cycles at 0.5 A g<sup>-1</sup> with an average CE of 99.3%) can be achieved in the AC (−)/graphite (+) full cell. Notably, a high energy density of 204 Wh kg<sup>-1</sup> (calculated on the active mass of both electrodes) is achieved. This exploration sheds light on the construction of novel LICs based on graphite cathode and demonstrates the potential to achieve electrochemical systems with high-performance energy storage capability through the assistance of anion intercalation chemistry.

## 2. Materials and Methods

### 2.1. Materials

Electrolyte: 1M LiPF<sub>6</sub> EC/EMC (1:1, vol.) and 1M LiPF<sub>6</sub> EMC were produced from Merck Life Science UK Limited. SLP50, SP1, and SFG6L graphite and Super P carbon black were sourced from IMERYS Graphite & Carbon (Switzerland). Lithium metal foil with a diameter of 16 mm and a thickness of 0.025 cm, along with polypropylene (PP) separator film, were obtained from Xiamen TOB New Energy Technology Co., Ltd (China). Sodium alginate (NaAl) was a product of MP Biomedicals. Commercial Ketjen Black (KB) was

purchased from Shandong Gelon Lib Co., Limited (China). The glass fibre membrane separator (MG 160) was acquired from Fisher Scientific UK Ltd. Commercial TF-B520 activated carbon was supplied by MTI Corporation (UK). All chemicals were used directly without undergoing any additional purification processes.

## 2.2. Experimental Procedures

### 2.2.1. Graphite and Activated Carbon Electrode Preparation

For preparation of the graphite and activated carbon electrode, SLP50 graphite, Ketjen Black, and sodium alginate (NaAl) binder were first mixed by deionised water using a speed mixer (SpeedMixer DAC 600.2, Artisan technology group, USA) in a mass ratio of 8:1:1. The homogeneous slurry was then cast onto carbon-coated Al foil as the current collector, and the electrode was dried in a vacuum oven at 80 °C overnight. The electrode discs of 12 mm in diameter with a mass loading of 1.8–2.2 mg were cut. The TF-B520 activated carbon electrode was prepared using CMC binder and carbon black (Super P) in a mass ratio of 7:1.5:1.5. The CMC binder was first dissolved by deionised water, and then, activated carbon and carbon black were added to form a homogeneous slurry. The paste was coated on the Cu foil, and the desired electrode (diameter of 15 mm) was obtained after drying at 80 °C overnight. The mass ratio between graphite and the activated carbon electrode was 2:1 in this work.

### 2.2.2. Cell Assembly and Electrochemical Testing of the Li//AC, Li//Graphite Half Cell, and AC (−)//Graphite (+) Cells

Cell assembly: The CR2032-type coin cells were used to assemble cells, while AC or graphite with the electrode and lithium metal (diameter 16 mm) was served as the counter/reference electrode, and the polypropylene separator film or glass fibre (diameter 18 mm) was used as the separator. The electrolytes for Li//AC and Li//graphite half cells were 1M LiPF<sub>6</sub> EC/EMC (1:1, vol.) and 1M LiPF<sub>6</sub> EMC (~120 µL), respectively. For the assembly of AC (−)//graphite (+) cells, the AC anode was first discharged/charged for 5 cycles in Li//AC half cells within 0.01–3.0 V at 100 mA g<sup>-1</sup>, then discharged to 0.01 V to the pre-lithiate. In the meantime, the graphite cathode was pre-cycled for 5 charge/discharge processes in Li//graphite half cells within 3.0–5.0 V at 100 mA g<sup>-1</sup>, then stopped at the upper cut-off voltage of 5.0 V. The coin cell configuration is displayed in Figure S1 (Supplementary Materials). The pre-prepared AC anode and graphite cathode were then assembled in a coin cell with a glass fibre separator, and the amount of electrolyte was ~150 µL. The assembly of coin cells was conducted in the glovebox with O<sub>2</sub> < 0.5 ppm and H<sub>2</sub>O < 0.5 ppm.

Electrochemical performance measurements: The galvanostatic charge/discharge test was performed with the NEWARE test system (BTS9000, Shenzhen, China), and the voltage ranges for the Li//AC, Li//graphite, and AC (−)//graphite (+) cells were 0.01–3.0 V, 3.0–5.0 V, and 2.0–5.0 V, respectively. Cyclic voltammetry (CV) was measured with the electrochemical workstation (VersaSTAT 4 Potentiostat Galvanostat, Ametek scientific instruments, USA).

### 2.2.3. Materials Characterisations

The morphologies of pristine graphite and activated carbon were examined by scanning electron microscope (SEM; TESCAN MIRA3 SC + OI EDS). The transmission electron microscope (TEM) images were acquired by Talos™ F200X TEM. X-ray diffraction (XRD) was conducted with an X-ray diffractometer (Powder X-ray Diffraction Phillips X'Pert) using Cu-K $\alpha$  radiation at a wavelength of 0.15418 nm ( $V = 30$  kV,  $I = 25$  mA). Raman measurement was carried out by a Renishaw inVia Reflex Raman microscope. The surface area was analysed by acquiring nitrogen absorption/desorption isotherms using the Brunauer–Emmett–Teller (BET) method on a Surface Area Analyzer—Quadasorb Evo.

### 3. Results and Discussion

#### 3.1. Half Cell Investigations

##### 3.1.1. Li // Graphite Half Cell via Anion Intercalation/De-Intercalation

Figure 1a shows the XRD pattern of SLP50 graphite, in which a strong peak located at  $26.35^\circ$  is observed. This reflection can be associated with the crystallographic (002) plane of graphite. The Raman spectrum of SLP50 graphite is exhibited in Figure 1b, appearing in three peaks positioned at 1335, 1580, and  $2686\text{ cm}^{-1}$ , which correspond to the D band, G band, and 2D band, respectively. The G band is the specific reflection for  $\text{sp}^2$  carbon networks, while the D band is the defect-induced Raman feature. The ratio of intensity  $I_{\text{D}}/I_{\text{G}}$  for the D and G bands is normally used for predicting the defect quantity and degree of graphitisation. The  $I_{\text{D}}/I_{\text{G}}$  for SLP50 graphite was calculated to be 0.256, suggesting few defects in the well-ordered graphitic structures. Figure 1c is the  $\text{N}_2$  adsorption/desorption isotherms, revealing the BET surface area for SLP50 graphite to be  $2.6\text{ m}^2/\text{g}$ . This relatively small surface suggests limited porosity or specific surface features. The pore size distribution is exhibited in Figure S2 (Supplementary Materials), indicating the presence of a small quantity of pores. The SEM technique was further employed to gain a more comprehensive understanding of the surface feature and morphology of SLP50 graphite. The SEM images are depicted in Figure 1d–f, and flake-shaped graphitic particles with a thickness of  $\sim 2\text{ }\mu\text{m}$  are observed, while the particle size distribution is mainly between the range of  $\sim 20$  to  $50\text{ }\mu\text{m}$ . Furthermore, the high-resolution TEM images are listed in Figure 1g,h, revealing detailed insights into the crystalline structure. The lattice distance for the (002) plane of SLP50 graphite was analysed to be  $\sim 0.338\text{--}0.346\text{ nm}$ , offers a suitable interlayer spacing that can effectively accommodate the intercalation of anions.

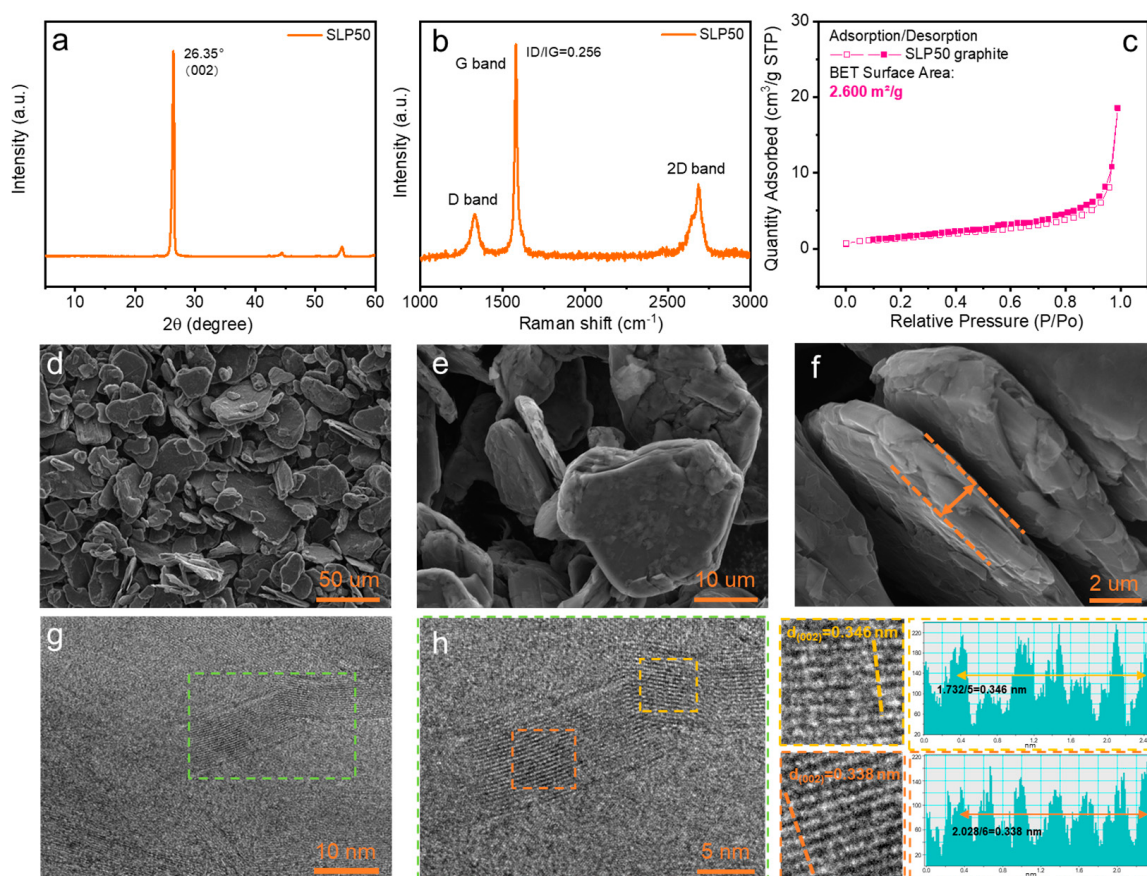


**Figure 1.** Characterisation of SLP50 graphite: (a) XRD; (b) Raman; (c)  $\text{N}_2$  adsorption/desorption isotherm; (d–f) SEM images; (g,h) high-resolution TEM images.

Figure 2 displays the testing results of electrochemical  $\text{PF}_6^-$  anion intercalation into SLP50 graphite in the Li//graphite half cells based on 1M  $\text{LiPF}_6$  EMC electrolyte. The  $\text{PF}_6^-$  anion intercalation/de-intercalation process was first analysed at a constant current density of  $100 \text{ mA g}^{-1}$  in the voltage range of 3.0–5.0 V. The galvanostatic charge/discharge curves for the initial three cycles are exhibited in Figure 2a. The charge platforms detected in the curves are associated with the “staging” process, which are identified as four potential regions of 4.44–4.51 V (stage I), 4.51–4.74 V (stage II), 4.74–4.92 V (stage III), and 4.92–5.0 V (stage IV), reflecting that the  $\text{PF}_6^-$  anions intercalate into graphite interlayers to form graphite intercalation compounds (GICs) [18]. Meanwhile, the anion de-intercalation platforms are observed in the discharge curves, revealing a reversible  $\text{PF}_6^-$  anion intercalation/de-intercalation process. Figure 2b shows the relevant capacitance differential ( $dQ/dV$ ) curves, while these specific peaks correspond to the charge/discharge plateaus in galvanostatic charge/discharge curves. The onset voltage for anion intake is around 4.44 V, and subsequent peaks confirm the occurrence of intercalation/de-intercalation processes at certain potentials. Figure 2c lists the evaluation of the specific capacity and Coulombic efficiency (CE) within 100 cycles. Importantly, a high discharge capacity of  $\sim 120 \text{ mAh g}^{-1}$  via this anion intercalation/de-intercalation process was achieved and was extremely stable after 100 repeated charge/discharge processes. The initial CE was 40% and increased from cycle to cycle until it was stable at  $\sim 90\%$ , and the small CE was due to the electrolyte degradation and self-discharge reactions at the high upper cut-off voltage. Figure 2d exhibits the specific capacity of Li//graphite half cells at a high current density of  $500 \text{ mA g}^{-1}$  in the voltage range of 3.0–5.0 V. The discharge capacity decreases slightly to  $\sim 100 \text{ mAh g}^{-1}$ , and the capacity retention after 2000 cycles is 82%, indicating the great long-term cyclic stability. This excellent cyclic capability of SLP50 graphite in a standard concentration electrolyte (1M  $\text{LiPF}_6$  EMC) is comparable to other reported graphite cathodes, even those using high-concentration electrolytes or ionic liquid electrolytes [19,20]. Figure 2e concludes the medium discharge voltage of the Li//graphite half cells, and the inset displays charge/discharge curves from the 100th to 2000th cycles. Notably, the medium discharge voltage was stable at  $\sim 4.5 \text{ V}$  after 2000 cycles, indicating excellent cyclic reversibility and stability. A slight decrease in the charge/discharge plateau voltage during the cycles further demonstrates less polarisation in the cell. Figure 2f presents the charge/discharge capacities of the Li//graphite half cells at different current densities. At the current densities of 0.1, 0.2, 0.4, 0.8, and  $1.0 \text{ A g}^{-1}$ , the discharge capacities of the cell were around  $100 \text{ mAh g}^{-1}$ , respectively, indicating great applicability with the current increasing. Figure S3 (Supplementary Materials) shows the cyclic voltammetry curves of the Li//graphite half cells at different scan rates, where the primary oxidation/reduction peaks are observed and retained well when the scan rate changes, revealing good reversibility of the electrode reaction. In addition, the capacity decayed to  $75 \text{ mAh g}^{-1}$  and then fell to  $70 \text{ mAh g}^{-1}$  when the current density increased to 1.5 and  $2.0 \text{ A g}^{-1}$ . This decrease in capacity under high current conditions is a consequence of larger concentration polarisation, hindering the electrode reactions and the effective capacity. Figure 2g shows the charge/discharge curves of the cell at different current densities. Correspondingly, the voltage hypothesis phenomenon was observed in the charge/discharge curves as the current densities increased, suggesting there was a noticeable deviation in the voltage behaviour. Notably, the discharge capacity was recovered to  $100 \text{ mAh g}^{-1}$  when the current density was reversed to  $1.0 \text{ A g}^{-1}$ , revealing a good reversibility of the Li//graphite cell. Moreover, the medium voltage and onset voltage for anion intercalation into graphite interlayers at different current densities are compared in Figure 2h. It is observed that the medium voltage was reversibly resumed to 4.51 V when the current density returned from  $2 \text{ A g}^{-1}$  to  $0.1 \text{ A g}^{-1}$ , suggesting good reversibility of the cell. The onset voltage for anion intercalation kept increasing when the current density was increased, which most likely contributed to the higher activation barrier resulting from the sluggish kinetic movement of  $\text{PF}_6^-$  at the large current condition [21]. These results demonstrate the effective interca-

lation and de-intercalation of  $\text{PF}_6^-$  anions in SLP50 graphite, suggesting the potential for the construction of a high-performance full-cell system.

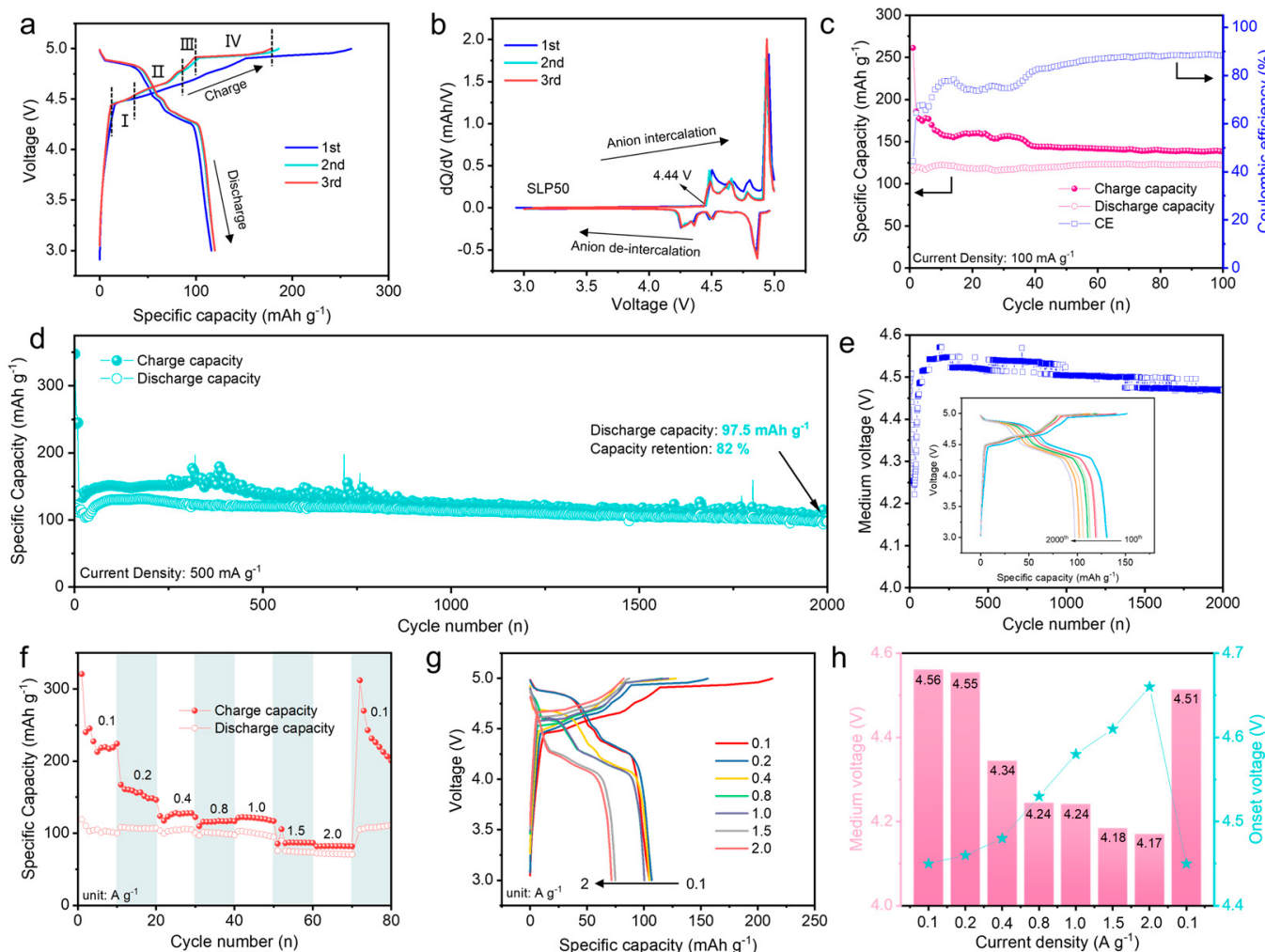


**Figure 2.** Electrochemical performances of Li//graphite half cells in 1M  $\text{LiPF}_6$  EMC electrolytes. (a) Galvanostatic charge/discharge curves for the initial three cycles and (b) relevant initial three capacitance differential ( $dQ/dV$ ) curves; (c) charge/discharge capacities and Coulombic efficiency at the current density of  $100 \text{ mA g}^{-1}$  within 100 cycles; (d) charge/discharge capacities at the current density of  $500 \text{ mA g}^{-1}$  within 2000 cycles; (e) medium voltage at different cycles, and the inset is the charge/discharge curves at the 100th–2000th cycles; (f) charge discharge capacities of the cells under various current densities from 0.1 to  $2.0 \text{ A g}^{-1}$ ; (g) relevant charge/discharge curves; (h) medium and onset voltage comparisons under different current densities.

### 3.1.2. Li//AC Half Cells via $\text{Li}^+$ Adsorption/Desorption

The crystallinity of TF-B520 activated carbon (AC) was conducted using XRD, and the pattern is exhibited in Figure 3a. The absence of a diffraction peak for the reflection of the graphite (002) plane is attributed to the lack of a well-defined long-range order in the arrangement of the carbon atom [22]. The broad and weak peak around  $43^\circ$  is observed in the spectrum, corresponding to the diffraction of the (100) plane, while the low intensity of the diffraction peak demonstrates the amorphous structures [23]. Figure 3b displays the Raman spectra of AC, while the D band ( $1345.7 \text{ cm}^{-1}$ ) and G band ( $1598.5 \text{ cm}^{-1}$ ) are clearly observed. The ID/IG was calculated as 0.93, indicating lower fractions of the graphitic region and the disordered nature of the carbon matrix. According to the  $\text{N}_2$  adsorption/desorption curves in Figure 3c, the BET surface area value for AC was

measured to be  $911.75 \text{ m}^2/\text{g}$ , which is much larger than that of SLP50 graphite. The pore size distribution, shown in Figure S4 (Supplementary Materials), highlights a prominent microporous structure with a pore size ranging from 0.5 to 0.8 nm. A larger surface area implies more adsorption sites, thus conferring a higher adsorption capacity. This facilitates rapid adsorption and desorption of ions on the AC electrode surface. Figure 3d,e show the SEM images of the AC, and the size is mainly distributed in the range of 5–10  $\mu\text{m}$ . Figure 3f illustrates the TEM image of the AC, revealing disordered microstructures characteristic of amorphous carbon.

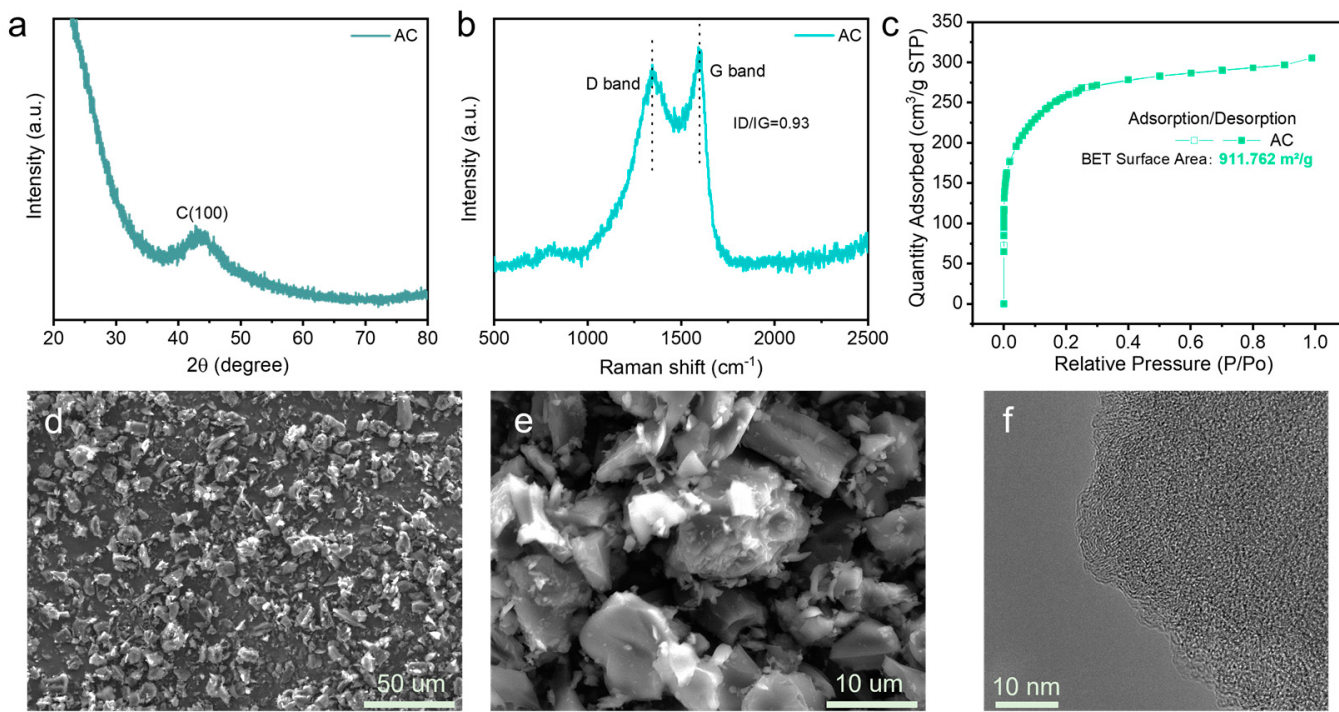


**Figure 3.** Characterisation of TF-B520 activated carbon: (a) XRD; (b) Raman; (c)  $\text{N}_2$  adsorption/desorption isotherm; (d,e) SEM images; (f) high-resolution TEM image.

The electrochemical performances of the AC electrode were investigated in Li//AC half cells with the electrolyte of 1M LiPF<sub>6</sub> EC/EMC (vol. 1:1). Figure 4a displays the initial five galvanostatic charge/discharge curves for the AC electrode at the current density of 100  $\text{mA g}^{-1}$  between the voltage range of 0.01–3.0 V. The first discharge capacity was found to be 1200  $\text{mAh g}^{-1}$ , which reduced to ~300  $\text{mAh g}^{-1}$  in the second cycle and was stable for five cycles. The long plateau in the first cycle is attributed to the formation of a solid electrolyte interphase (SEI) film on the AC electrode surface. Figure 4b illustrates the specific charge/discharge capacities and CE of the cell at 100  $\text{mA g}^{-1}$  in different cycles. The discharge capacity was kept at ~260  $\text{mAh g}^{-1}$  after 200 repeated charge/discharge processes, indicating an excellent cyclic stability. Figure 4c shows the charge/discharge capacities and CE of the cell at a large current density of 500  $\text{mA g}^{-1}$  after the initial 10 formation cycles at 100  $\text{mA g}^{-1}$ . The capacity was maintained above 200  $\text{mAh g}^{-1}$  after 1000 cycles, yielding a CE near 99.7%. Notably, a good cyclic capability was confirmed by the overlapped charge/discharge curves of the cells at different cycles from the 100th to 1000th (Figure 4d). CV analysis of the Li//AC cell was first conducted at the scan rate of 0.1  $\text{mV s}^{-1}$ , and the initial four cycle CV curves are exhibited in Figure 4e. It is obvious that the typical broad peak between 0.5 and 1.0 V is observed for each cycle, probably due to a formation of the SEI layer on the AC electrode surface. The strong current drop below the voltage of 0.5 V is associated with the reaction between  $\text{Li}^+$  and the AC electrode. Furthermore, the CV analysis at various scan rates (0.2, 0.5, 0.8, 1.0, and 2.0  $\text{mV s}^{-1}$ ) was carried out to investigate the electrochemical dynamic behaviour of the electrode, and

the curves are depicted in Figure 4f. As the scan rate increases, the peak intensity of the electrode reaction rises, resulting from an augmented electrochemical reaction rate. Notably, according to previous reports, the electrochemical storage behaviour can be specified by the equations as follows [24–26]:

$$i = av^b \quad (2)$$

$$\log(i) = b\log(v) + \log a \quad (3)$$

$$i = k_1v + k_2v^{1/2} \quad (4)$$

$$i/v^{1/2} = k_1v^{1/2} + k_2 \quad (5)$$

where  $i$  is the current,  $v$  is the scan rate, and  $a$  and  $b$  are the variable parameters. The  $b$ -value, determined from the slope of  $\log(i)$  versus  $\log(v)$  plot, approaches 0.5 when diffusion-controlled behaviours are predominant. Conversely, a  $b$ -value close to 1.0 signifies the dominance of pseudocapacitive contributions. Figure 4g shows the fitted relationship between  $\log(i)$  and  $\log(v)$  of the AC electrode at different voltages. The corresponding  $b$ -values when discharged to 1.0 and 0.8 V and charged to 0.8 and 1.0 V are calculated to be 0.92, 0.86, 0.96, and 1.0, respectively. The  $b$ -value approaching 1 indicates the surface-induced capacitive behaviour of the AC electrode, revealing efficient electrode reaction kinetics. Based on Equations (4) and (5), the current ( $i$ ) is expressed as the sum of  $k_1v$  and  $k_2v^{1/2}$  at specific voltages corresponding to the capacitive behaviour and diffusion-controlled behaviour, respectively. The value of  $k_1$  can be determined by plotting the curve with  $i/v^{1/2}$  versus  $v^{1/2}$ , and the capacitive contribution is the value of  $k_1v$ . Figure 4h quantitatively analyses the surface-dominated contribution, revealing that 65.45% of the whole capacity belongs to the non-diffusion controlled capacity at the scan rate of  $2 \text{ mV s}^{-1}$ . Clearly, it is found that the diffusion-controlled behaviours mainly contribute to the whole discharge capacity in the reduction range between 0.75 and 0.01 V, suggesting a  $\text{Li}^+$  intake process occurring on the electrode at low voltage. This behaviour is similar to that of previously reported electrode materials [27,28]. Moreover, as shown in Figure 4i, the percentage for capacitive contributions of the AC electrode exhibits an increasing trend when the scan rate rises, disclosing the more dominated capacitive behaviour at high rates.

### 3.2. AC (−)/Graphite (+) Full-Cell Investigations

#### 3.2.1. Cell Configuration

The full-cell configuration of AC (−)/graphite (+) is achieved by employing an AC anode and graphite cathode. Scheme 1 illustrates a comparison of the three capacitors mentioned above (supercapacitor, conventional LICs with an AC cathode, and LICs with a graphite cathode). In these novel LICs with a graphite cathode,  $\text{PF}_6^-$  anions are forced to intercalate into graphite interlayers during the charging process, while  $\text{Li}^+$  ions are absorbed onto the AC surface. Conversely, during the discharging process,  $\text{PF}_6^-$  anions and  $\text{Li}^+$  ions are released and return to the electrolyte. Here, a pre-lithiation process is necessary for the AC anode to enhance the availability of  $\text{Li}^+$  ions for charge storage and facilitate the effective formation of SEI film. The charge/discharge curves for the pre-lithiation process of the AC anode are displayed in Figure S5a (Supplementary Materials). Additionally, a pre-cycle treatment is applied to the graphite cathode to activate the anion intercalation pathways, with the charge/discharge curves of the  $\text{Li}^+/\text{graphite}$  half cells shown in Figure S5b (Supplementary Materials). The AC and graphite electrodes are fully discharged and fully charged to 0.01 V and 5 V, respectively, allowing for  $\text{Li}^+$  absorption and  $\text{PF}_6^-$  anions intercalation, before being used to assemble the full cell.

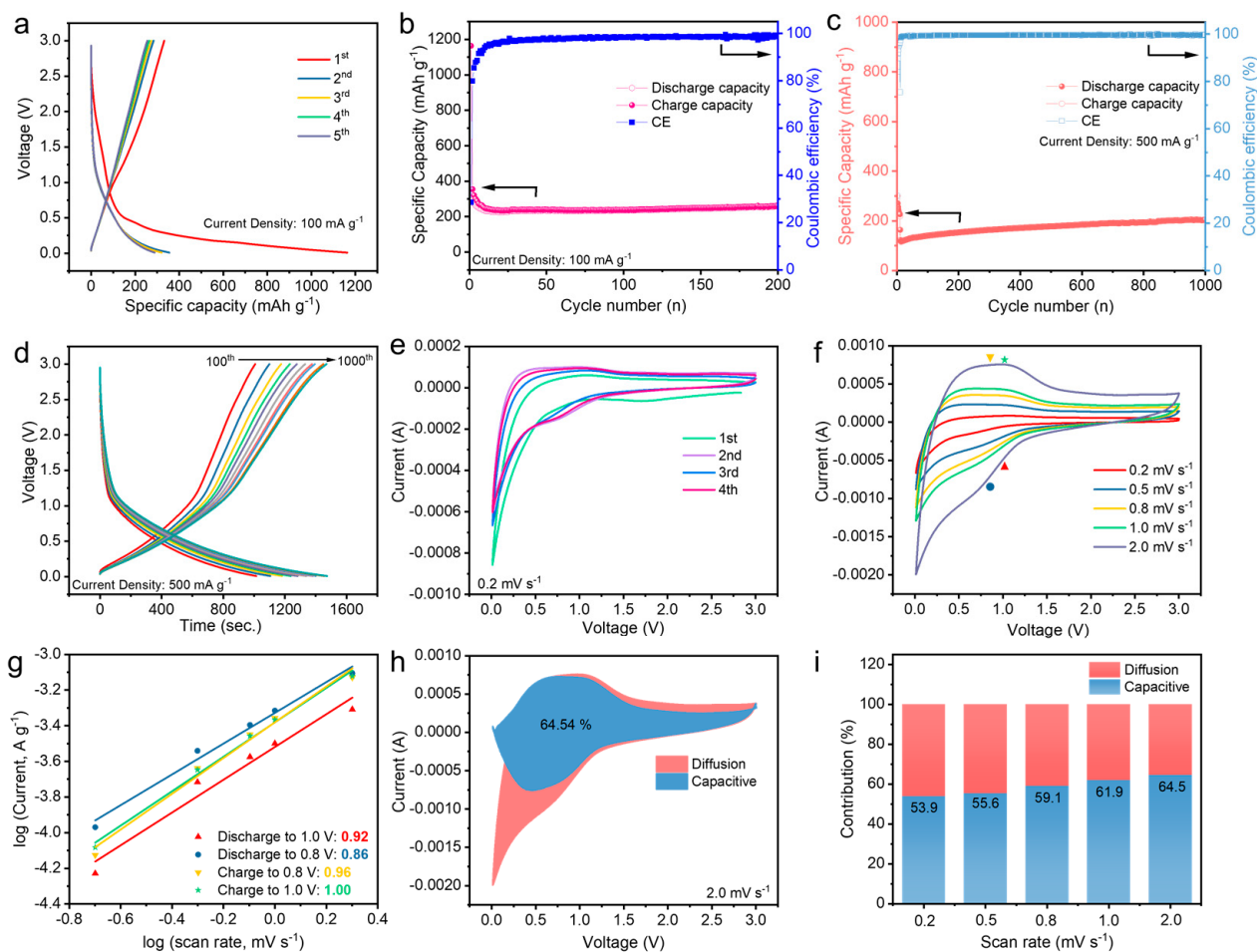
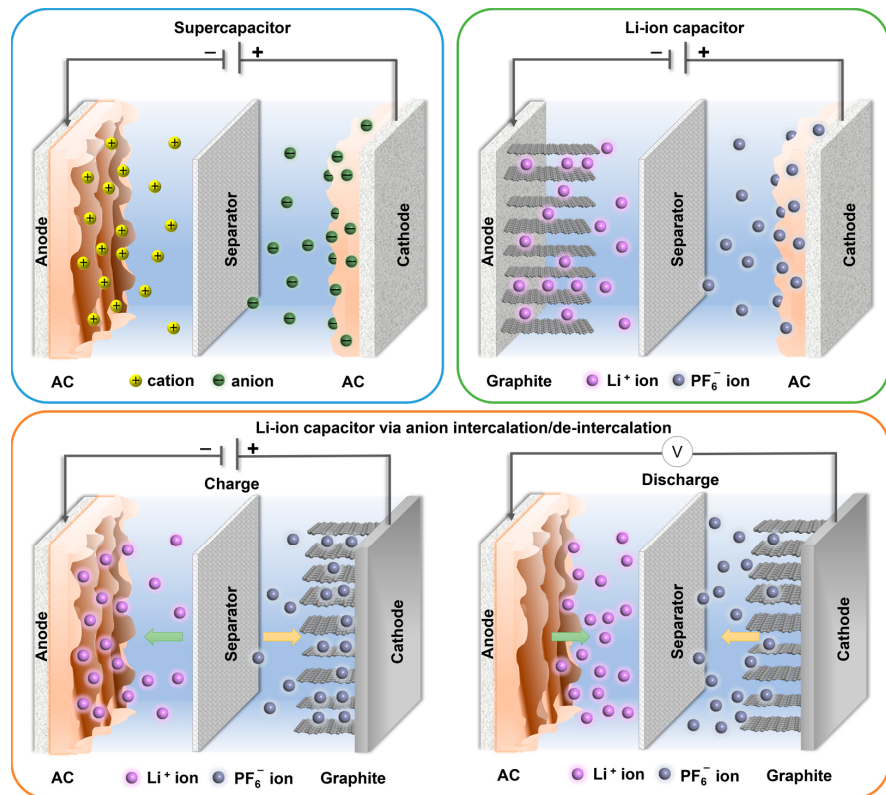


**Figure 4.** Electrochemical performances of Li//AC half cells in 1M LiPF<sub>6</sub> EC/EMC (vol. 1:1) electrolytes. (a) Galvanostatic charge/discharge curves for the initial five cycles, and (b) charge/discharge capacities and Coulombic efficiency at the current density of 100 mA g<sup>-1</sup> within 200 cycles; (c) charge/discharge capacities at the current density of 500 mA g<sup>-1</sup> within 1000 cycles, and (d) relevant charge/discharge curves at different cycles; (e) initial four CV curves at the scan rate of 0.1 mV s<sup>-1</sup>; (f) CV curves at various scan rates of 0.2, 0.5, 0.8, 1.0, and 2.0 mV s<sup>-1</sup>; (g) the linear relation between log(*i*) and log(*v*); (h) pseudocapacitive contributions (blue) and diffusion-controlled contributions (pink) at the scan rate of 2.0 mV s<sup>-1</sup>; (i) ratios of capacitive and diffusion charge storage to the total charge storage at different scan rates.

### 3.2.2. Electrochemical Performances

The electrochemical performance of AC (−)/graphite (+) full cells was first investigated by the galvanostatic charge/discharge test. Figure 5a displays the initial five charge/discharge curves of the cell at the current density of 100 mA g<sup>-1</sup> with the voltage range between 2.0 and 5.0 V. It is clear that the voltage plateaus corresponding to the anion intercalation behaviour are observed. The charge capacity of the first cycle reaches 90 mAh g<sup>-1</sup>, but the first discharge capacity is lower than 50 mAh g<sup>-1</sup>, yielding an initial CE of 50%. The lower CE in the first cycle is probably associated with the parasitic reactions, such as the electrolyte decomposition and self-discharge behaviour. Notably, the subsequent curves are overlapped well, which demonstrates the excellent cyclic reversibility and stability. Correspondingly, the initial five dQ/dV curves are exhibited in Figure 5b, while the peaks are attributed to the plateaus in the charge/discharge curves. The onset voltage for anion intercalation in the first cycle is 3.95 V, and the voltage decreases to 3.81 V in the second cycle and 3.76 V for subsequent cycles. The shift in the onset voltage indicates that the first uptake of anions into graphite interlayers needs to overcome the

activation barrier to open the interlayer gaps [21,29,30]. This onset shift is also observed in CV curves of the cell at the scan rate of  $0.2 \text{ mV s}^{-1}$  (Figure S6a, Supplementary Materials). Meanwhile, the specific peaks observed in the CV curves are associated with the anion intercalation/de-intercalation behaviours. Moreover, Figure S6b (Supplementary Materials) exhibits CV curves at various scan rates from  $0.2$  to  $2.0 \text{ mV s}^{-1}$ , and good reversibility of the cell is demonstrated. Figure 5c exhibits the charge/discharge capacities and relevant CE of the AC (−)/graphite (+) cell at the current density of  $100 \text{ mA g}^{-1}$  between the voltage range of  $2.0\text{--}5.0 \text{ V}$  within the 200 cycles. The discharge capacity of  $45 \text{ mAh g}^{-1}$  is delivered after 200 repeated charge/discharge processes, yielding a CE of 91.4%. The capacity retention of the cell is higher than 90%, demonstrating an excellent cyclic stability. The cyclic stability of the AC (−)/graphite (+) cell was further explored through the galvanostatic charge/discharge cycle at a high current density of  $500 \text{ mA g}^{-1}$ . The charge/discharge capacities and CE for 5000 cycles are exhibited in Figure 5d. Obviously, the capacity was still stable after 5000 cycles, yielding a capacity retention of 87.5% with an average CE of 99.3%. Furthermore, as shown in Figure 5e, the reversible discharge capacities of  $48.7$ ,  $46.1$ ,  $41.0$ ,  $33.5$ ,  $31.4$ ,  $27.4$ , and  $26.3 \text{ mAh g}^{-1}$  are maintained at various current densities of  $0.1$ ,  $0.2$ ,  $0.5$ ,  $0.8$ ,  $1.0$ ,  $1.5$ , and  $2.0 \text{ A g}^{-1}$ , respectively. Particularly, the capacity of the AC (−)/graphite (+) cell recovered to  $47.6 \text{ mAh g}^{-1}$  when the current density was switched back to the initial  $0.1 \text{ A g}^{-1}$ , exhibiting excellent rate capability and cyclic reversibility. Figure S7a (Supplementary Materials) displays the charge/discharge curves of the cell cycled at various current densities. Obviously, the discharge time reduces with the increasing current density. Figure S7b (Supplementary Materials) illustrates the medium voltage of the cell at various current densities, while the medium voltage drops from  $4.2 \text{ V}$  to  $3.8 \text{ V}$  when the current density increases from  $0.1$  to  $2.0 \text{ A g}^{-1}$ . This result demonstrates a high operating voltage in the AC (−)/graphite (+) full-cell system.



**Scheme 1.** The comparison among the conventional supercapacitor (AC//AC symmetric configuration), Li-ion capacitor (graphite (−)//AC (+) asymmetric configuration), and Li-ion capacitor via anion intercalation (AC (−)//graphite (+) configuration).

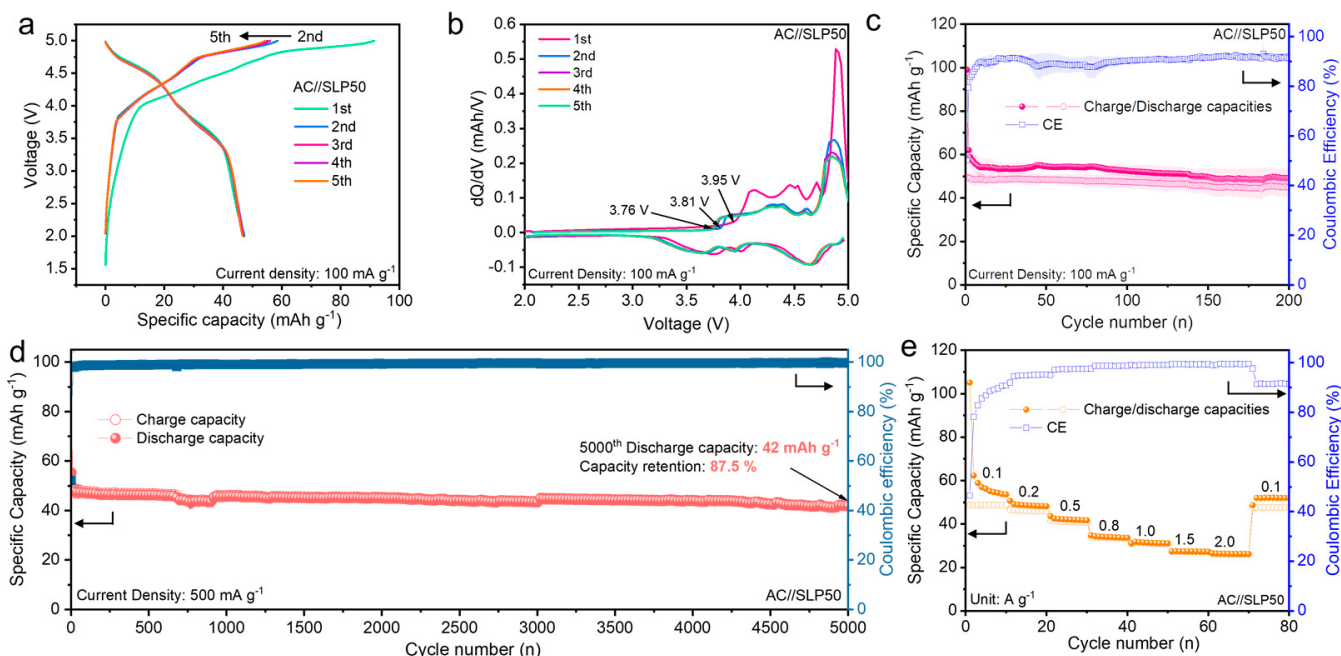


**Figure 5.** Electrochemical performances of the AC (−)/graphite (+) full cell in 1M LiPF<sub>6</sub> EMC electrolytes. (a) Galvanostatic charge/discharge curves for the initial five cycles and (b) relevant dQ/dV curves; (c) charge/discharge capacities and CE at the current density of 100 mA g<sup>−1</sup> within 200 cycles; (d) charge/discharge capacities and CE at current density of 500 mA g<sup>−1</sup> within 5000 cycles; (e) rate performances at different current densities of 0.1, 0.2, 0.5, 0.8, 1.0, 1.5, and 2.0 A g<sup>−1</sup>.

Accordingly, the energy and power density of the AC (−)/graphite (+) full-cell system were calculated using the equations provided in the Supplementary Materials, with detailed data displayed in Table S1 (Supplementary Materials). The comparisons, shown in the Ragone plot in Figure 6a and Table S2 (Supplementary Materials), are displayed with the previously fabricated LICs. A high energy density of 204 Wh kg<sup>−1</sup> (calculated based on the active mass of both electrodes) is achieved at a power density of 418 W kg<sup>−1</sup>. At a high power density of 7.7 kW kg<sup>−1</sup>, the AC (−)/SLP50 graphite (+) full cell delivers an energy density of 100 Wh kg<sup>−1</sup>, exceeding most LICs based on anion absorption/desorption on the surface of the AC cathode [9,31–40]. Additionally, the electrochemical performance of this AC (−)/SLP50 graphite (+) full-cell system is compared to reported dual-graphite battery systems [41–50]. The comparison of the cycle life, capacity retention, and average Coulombic efficiency is presented in Figure 6b, with the detailed data summarised in Table S3. Notably, the novel AC (−)/SLP50 graphite (+) full-cell system in this work demonstrates a prolonged cycle life, along with cyclic efficiency and capacity retention comparable to those of dual-graphite batteries.

Moreover, different types of graphite, including SP1 and SFG6L, were applied as cathodes in the AC (−)/graphite (+) full-cell system. The detailed physical properties of these two graphite types are displayed in Figure S8 (Supplementary Materials). Figure S9 (Supplementary Materials) exhibits the electrochemical performance of the full cell, demonstrating a reversible and stable cyclic capability for both AC (−)/SP1 graphite (+) and AC (−)/SFG6L graphite (+) configurations. In summary, it can be concluded that various graphite cathode materials are suitable for this novel AC (−)/graphite (+) system in the electrolyte of 1 M LiPF<sub>6</sub> EMC operating at a high voltage range. This demonstrates the compatibility of graphite cathodes with anion intercalation behaviour for the improvement in the overall performances of AC-based energy storage devices. Notably, the electrochemical performance varies with different types of graphite. The potential influence of graphite properties on the overall performance of this AC (−)/graphite (+) full-cell system will be explored in our future work.

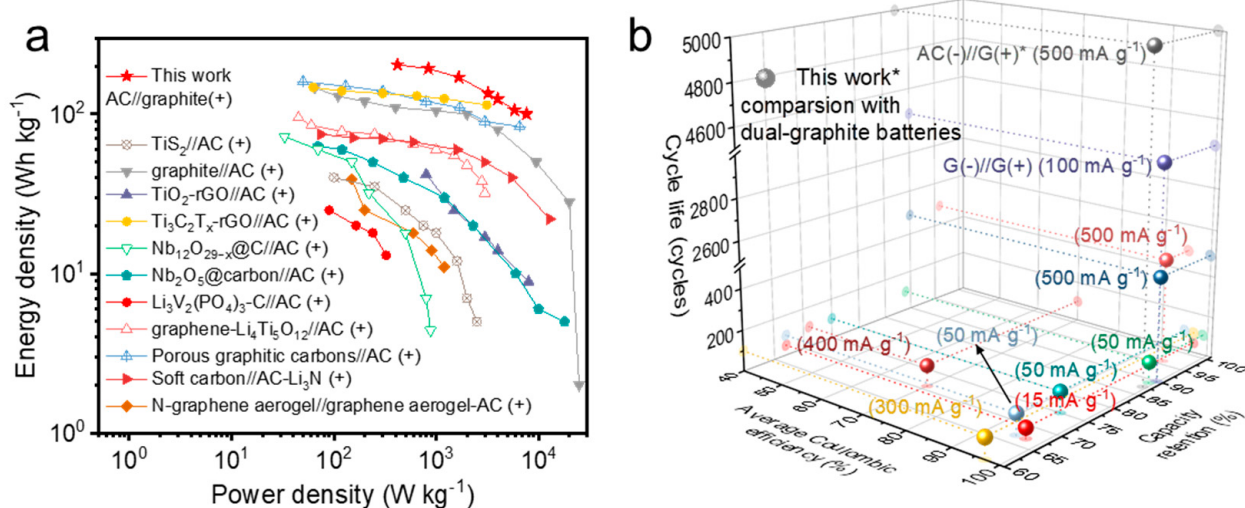


**Figure 6.** Comparison of performances of the AC (−)/graphite (+) full cell in this work with reported works. (a) Ragone plot of the AC (−)/graphite (+) full cell in this work, and comparison with previously fabricated LICs in the literature. (b) Cyclic performances of the AC (−)/graphite (+) full cell in this work compared with reported dual-graphite batteries.

#### 4. Conclusions

In summary, we demonstrated graphite as the cathode material for a novel AC (−)/graphite (+) device with the assistance of anion intercalation/de-intercalation chemistry. It has been found that the graphite cathode storing an anion charge via intercalation behaviour can deliver a higher capacitance than the commercial AC based on surface adsorption. The as-designed AC (−)/graphite (+) device showed a high energy density (>200 Wh kg<sup>-1</sup>) with a well-maintained power density (>7 kW kg<sup>-1</sup>), surpassing most reported supercapacitors and LICs. The AC (−)/graphite (+) device was also evaluated by cyclic stability and rate capability, which achieved a high capacity retention of 87.5% after 5000 cycles at the current density of 0.5 A g<sup>-1</sup>, yielding an average CE of 99.3%. Moreover, various commercial graphite with different properties were successfully applied in this AC (−)/graphite (+) system, demonstrating good compatibility. Considering the abundance, wide availability, and low cost of the commercial graphite, this work is expected to inspire the development of novel electrochemical devices with a prolonged cyclic life, high energy density, and fast energy conversion rates.

**Supplementary Materials:** The following supporting information can be downloaded at <https://www.mdpi.com/article/10.3390/batteries10090296/s1>: Figure S1. The coin cell construction for (a) Li//AC or Li//graphite half cells and (b) AC (−)/graphite (+) full cell. Figure S2. Pore size distribution of SLP50 graphite. Figure S3. The cyclic voltammetry curves of the Li//graphite half cells at different scan rates. Figure S4. Pore size distribution of TF-B520 activated carbon. Figure S5. (a) The charge/discharge curves for (a) the pre-lithiation process of Li//AC half cells, and (b) the pre-cycle treatment of Li//graphite half cells. Figure S6. (a) Initial three CV curves of the AC (−)//SLP50 (+) full cell at the scan rate of 0.1 mV s<sup>-1</sup>, and (b) CV curves of the cell at different scan rates. Figure S7. (a) Charge/discharge curves of the AC (−)//SLP50 (+) full cell cycled at various current densities. (b) Medium voltage of the cell at various current densities. Table S1. Energy density and power density of the AC (−)//SLP50 graphite (+) full cell. Table S2. Comparison of the energy and power densities of the AC (−)//SLP50 graphite (+) full cell with reported AC cathode-based LICs. Table S3. Comparison of the electrochemical performance of the AC (−)//SLP50 graphite (+) full cell with reported dual-graphite batteries (G(-)/G(+)). Figure S8. (a,b) SEM images and (c) Raman spectrum of SP1 graphite, and (d,e) SEM images and (f) Raman spectrum of SFG6L graphite. Figure S9. (a) Charge/discharge capacities and CE at current density of 100 mA g<sup>-1</sup> within 500 cycles, (b) rate performance at various current densities, and (c) charge/discharge capacities and CE at current density of 500 mA g<sup>-1</sup> within 3000 cycles of AC (−)//SP1 (+) and AC (−)//SFG6L (+) full cells.

**Author Contributions:** Y.Z.: Conceptualisation, Methodology, Validation, Formal analysis, Investigation, Data curation, and Writing—original draft. J.L.: Formal analysis and Investigation. P.X.: Resources, Writing—review and editing, Supervision, and Project administration. All authors have read and agreed to the published version of the manuscript.

**Funding:** This work was supported by the China Scholarship Council/University of Manchester award. Ping Xiao acknowledges financial support from the Royal Academy of Engineering and Rolls-Royce for appointment of the Rolls-Royce/Royal Academy of Engineering Research Chair in Advanced Coating Technology.

**Data Availability Statement:** Data will be made available on request.

**Conflicts of Interest:** The authors declare that they have no known competing financial interests or personal relationships that could have appeared to influence the work reported in this paper.

## References

- Zou, K.; Deng, W.; Silvester, D.S.; Zou, G.; Hou, H.; Banks, C.E.; Li, L.; Hu, J.; Ji, X. Carbonyl Chemistry for Advanced Electrochemical Energy Storage Systems. *ACS Nano* **2024**, *18*, 19950–20000. [[CrossRef](#)]
- Liu, J.; Wang, J.; Xu, C.; Jiang, H.; Li, C.; Zhang, L.; Lin, J.; Shen, Z.X. Advanced Energy Storage Devices: Basic Principles, Analytical Methods, and Rational Materials Design. *Adv. Sci.* **2018**, *5*, 1700322. [[CrossRef](#)] [[PubMed](#)]
- Zou, K.; Jiang, M.; Ning, T.; Tan, L.; Zheng, J.; Wang, J.; Ji, X.; Li, L. Thermodynamics-directed bulk/grain-boundary engineering for superior electrochemical durability of Ni-rich cathode. *J. Energy Chem.* **2024**, *97*, 321–331. [[CrossRef](#)]
- Khan, F.M.N.U.; Rasul, M.G.; Sayem, A.S.M.; Mandal, N. Maximizing energy density of lithium-ion batteries for electric vehicles: A critical review. *Energy Rep.* **2023**, *9*, 11–21. [[CrossRef](#)]
- Divya, M.L.; Natarajan, S.; Lee, Y.S.; Aravindan, V. Biomass-Derived Carbon: A Value-Added Journey Towards Constructing High-Energy Supercapacitors in an Asymmetric Fashion. *ChemSusChem* **2019**, *12*, 4353–4382. [[CrossRef](#)]
- Wang, G.; Oswald, S.; Löffler, M.; Müllen, K.; Feng, X. Beyond Activated Carbon: Graphite-Cathode-Derived Li-Ion Pseudocapacitors with High Energy and High Power Densities. *Adv. Mater.* **2019**, *31*, 1807712. [[CrossRef](#)]
- Zhang, S.; Li, C.; Zhang, X.; Sun, X.; Wang, K.; Ma, Y. High Performance Lithium-Ion Hybrid Capacitors Employing Fe<sub>3</sub>O<sub>4</sub>-Graphene Composite Anode and Activated Carbon Cathode. *ACS Appl. Mater. Interfaces* **2017**, *9*, 17136–17144. [[CrossRef](#)]
- Eleri, O.E.; Lou, F.; Yu, Z. Lithium-Ion Capacitors: A Review of Strategies toward Enhancing the Performance of the Activated Carbon Cathode. *Batteries* **2023**, *9*, 533. [[CrossRef](#)]
- Khomenko, V.; Raymundo-Piñero, E.; Béguin, F. High-energy density graphite/AC capacitor in organic electrolyte. *J. Power Sources* **2008**, *177*, 643–651. [[CrossRef](#)]
- Sun, H.; Mei, L.; Liang, J.; Zhao, Z.; Lee, C.; Fei, H.; Ding, M.; Lau, J.; Li, M.; Wang, C.; et al. Three-dimensional holey-graphene/niobia composite architectures for ultrahigh-rate energy storage. *Science* **2017**, *356*, 599–604. [[CrossRef](#)]
- Kim, H.S.; Cook, J.B.; Lin, H.; Ko, J.S.; Tolbert, S.H.; Ozolins, V.; Dunn, B. Oxygen vacancies enhance pseudocapacitive charge storage properties of MoO<sub>3-x</sub>. *Nat. Mater.* **2017**, *16*, 454–462. [[CrossRef](#)] [[PubMed](#)]
- Zhang, L.; Wang, H.; Zhang, X.; Tang, Y. A Review of Emerging Dual-Ion Batteries: Fundamentals and Recent Advances. *Adv. Funct. Mater.* **2021**, *31*, 2010958. [[CrossRef](#)]
- Xiang, W.; Chen, M.; Zhou, X.; Chen, J.; Huang, H.; Sun, Z.; Lu, Y.; Zhang, G.; Wen, X.; Li, W. Highly Enforced Rate Capability of a Graphite Anode via Interphase Chemistry Tailoring Based on an Electrolyte Additive. *J. Phys. Chem. Lett.* **2022**, *13*, 5151–5159. [[CrossRef](#)]
- Wang, G.; Yu, M.; Wang, J.; Li, D.; Tan, D.; Löffler, M.; Zhuang, X.; Müllen, K.; Feng, X. Self-Activating, Capacitive Anion Intercalation Enables High-Power Graphite Cathodes. *Adv. Mater.* **2018**, *30*, 1800533. [[CrossRef](#)]
- Gao, J.; Tian, S.; Qi, L.; Yoshio, M.; Wang, H. Hexafluorophosphate intercalation into graphite electrode from gamma-butyrolactone solutions in activated carbon/graphite capacitors. *J. Power Sources* **2015**, *297*, 121–126. [[CrossRef](#)]
- Yoshio, M.; Nakamura, H.; Wang, H. Novel megallo-capacitance capacitor based on graphitic carbon cathode. *Electrochim. Solid-State Lett.* **2006**, *9*, 561–563. [[CrossRef](#)]
- Rajalekshmi, A.R.; Divya, M.L.; Lee, Y.S.; Aravindan, V. High-performance Li-ion capacitor via anion-intercalation process. *Batter. Energy* **2022**, *1*, 2021005. [[CrossRef](#)]
- Ji, B.; Zhang, F.; Song, X.; Tang, Y. A Novel Potassium-Ion-Based Dual-Ion Battery. *Adv. Mater.* **2017**, *29*, 1700519. [[CrossRef](#)]
- Beltrop, K.; Qi, X.; Hering, T.; Röser, S.; Winter, M.; Placke, T. Enabling bis(fluorosulfonyl)imide-based ionic liquid electrolytes for application in dual-ion batteries. *J. Power Sources* **2018**, *373*, 193–202. [[CrossRef](#)]
- Wu, L.N.; Peng, J.; Sun, Y.K.; Han, F.M.; Wen, Y.F.; Shi, C.G.; Fan, J.J.; Huang, L.; Li, J.T.; Sun, S.G. High-Energy Density Li metal Dual-Ion Battery with a Lithium Nitrate-Modified Carbonate-Based Electrolyte. *ACS Appl. Mater. Interfaces* **2019**, *11*, 18504–18510. [[CrossRef](#)]
- Placke, T.; Fromm, O.; Lux, S.F.; Bieker, P.; Rothermel, S.; Meyer, H.-W.; Passerini, S.; Winter, M. Reversible Intercalation of Bis(trifluoromethanesulfonyl)imide Anions from an Ionic Liquid Electrolyte into Graphite for High Performance Dual-Ion Cells. *J. Electrochem. Soc.* **2012**, *159*, A1755–A1765. [[CrossRef](#)]

22. Luo, X.F.; Yang, C.H.; Peng, Y.Y.; Pu, N.W.; Der Ger, M.; Hsieh, C.T.; Chang, J.K. Graphene nanosheets, carbon nanotubes, graphite, and activated carbon as anode materials for sodium-ion batteries. *J. Mater. Chem. A* **2015**, *3*, 10320–10326. [[CrossRef](#)]
23. Zięzio, M.; Charmas, B.; Jedynak, K.; Hawryluk, M.; Kucio, K. Preparation and characterization of activated carbons obtained from the waste materials impregnated with phosphoric acid(V). *Appl. Nanosci.* **2020**, *10*, 4703–4716. [[CrossRef](#)]
24. Zou, K.; Cai, P.; Liu, C.; Li, J.; Gao, X.; Xu, L.; Zou, G.; Hou, H.; Liu, Z.; Ji, X. A kinetically well-matched full-carbon sodium-ion capacitor. *J. Mater. Chem. A* **2019**, *7*, 13540–13549. [[CrossRef](#)]
25. Ge, P.; Li, S.; Xu, L.; Zou, K.; Gao, X.; Cao, X.; Zou, G.; Hou, H.; Ji, X. Hierarchical Hollow-Microsphere Metal–Selenide@Carbon Composites with Rational Surface Engineering for Advanced Sodium Storage. *Adv. Energy Mater.* **2019**, *9*, 1803035. [[CrossRef](#)]
26. Tan, L.; Huang, X.; Yin, T.; Guo, Y.; Ning, T.; Mei, Y.; Zou, K.; Li, L.; Ji, X.; Zou, G. A 5 V ultrahigh energy density lithium metal capacitor enabled by the fluorinated electrolyte. *Energy Storage Mater.* **2024**, *71*, 103692. [[CrossRef](#)]
27. Tan, X.; Zhang, F.; Chen, D.; Wang, P.; Liu, Y.; Meng, C.; Zhang, Y. Modulating NH<sub>4</sub><sup>+</sup> in vanadium oxide framework for high-efficient aqueous NH<sub>4</sub><sup>+</sup> storage. *Chem. Eng. J.* **2024**, *489*, 151119. [[CrossRef](#)]
28. Sun, L.; Zhang, Y.; Si, H.; Zhang, Y.; Liu, J.; Liu, J.; Zhang, Y. TiO<sub>2</sub>-modified red phosphorus nanosheets entangled in carbon nanotubes for high performance lithium ion batteries. *Electrochim. Acta* **2019**, *297*, 319–327. [[CrossRef](#)]
29. Balabajew, M.; Reinhardt, H.; Bock, N.; Duchardt, M.; Kachel, S.; Hampp, N.; Roling, B. In-Situ Raman Study of the Intercalation of Bis(trifluoromethylsulfonyl)imid Ions into Graphite inside a Dual-Ion Cell. *Electrochim. Acta* **2016**, *211*, 679–688. [[CrossRef](#)]
30. Lu, Y.; Zhang, D.; Wang, L.; Xu, M.; Song, J.; Goodenough, J.B. Electrochemical Behavior of a Graphite Electrode Prepared by Anodic Electrophoretic Deposition. *J. Electrochem. Soc.* **2012**, *159*, A321–A324. [[CrossRef](#)]
31. Satish, R.; Aravindan, V.; Ling, W.C.; Madhavi, S. Carbon-coated Li<sub>3</sub>V<sub>2</sub>(PO<sub>4</sub>)<sub>3</sub> as insertion type electrode for lithium-ion hybrid electrochemical capacitors: An evaluation of anode and cathodic performance. *J. Power Sources* **2015**, *281*, 310–317. [[CrossRef](#)]
32. Kim, H.; Cho, M.Y.; Kim, M.H.; Park, K.Y.; Gwon, H.; Lee, Y.; Roh, K.C.; Kang, K. A novel high-energy hybrid supercapacitor with an anatase TiO<sub>2</sub>-reduced graphene oxide anode and an activated carbon cathode. *Adv. Energy Mater.* **2013**, *3*, 1500–1506. [[CrossRef](#)]
33. Leng, K.; Zhang, F.; Zhang, L.; Zhang, T.; Wu, Y.; Lu, Y.; Huang, Y.; Chen, Y. Graphene-based Li-ion hybrid supercapacitors with ultrahigh performance. *Nano Res.* **2013**, *6*, 581–592. [[CrossRef](#)]
34. Li, G.; Yin, Z.; Guo, H.; Wang, Z.; Yan, G.; Yang, Z.; Liu, Y.; Ji, X.; Wang, J. Metalorganic Quantum Dots and Their Graphene-Like Derivative Porous Graphitic Carbon for Advanced Lithium-Ion Hybrid Supercapacitor. *Adv. Energy Mater.* **2019**, *9*, 1802878. [[CrossRef](#)]
35. Wang, X.; Wang, Z.; Zhang, X.; Peng, H.; Xin, G.; Lu, C.; Zhong, Y.; Wang, G.; Zhang, Y. Nitrogen-Doped Defective Graphene Aerogel as Anode for all Graphene-Based Lithium Ion Capacitor. *ChemistrySelect* **2017**, *2*, 8436–8445. [[CrossRef](#)]
36. Lim, E.; Jo, C.; Kim, H.; Kim, M.H.; Mun, Y.; Chun, J.; Ye, Y.; Hwang, J.; Ha, K.S.; Roh, K.C.; et al. Facile Synthesis of Nb<sub>2</sub>O<sub>5</sub>@Carbon Core-Shell Nanocrystals with Controlled Crystalline Structure for High-Power Anodes in Hybrid Supercapacitors. *ACS Nano* **2015**, *9*, 7497–7505. [[CrossRef](#)] [[PubMed](#)]
37. Chaturvedi, A.; Hu, P.; Aravindan, V.; Kloc, C.; Madhavi, S. Unveiling two-dimensional TiS<sub>2</sub> as an insertion host for the construction of high energy Li-ion capacitors. *J. Mater. Chem. A* **2017**, *5*, 9177–9181. [[CrossRef](#)]
38. Sun, C.; Zhang, X.; Li, C.; Wang, K.; Sun, X.; Ma, Y. High-efficiency sacrificial prelithiation of lithium-ion capacitors with superior energy-storage performance. *Energy Storage Mater.* **2020**, *24*, 160–166. [[CrossRef](#)]
39. Yi, S.; Wang, L.; Zhang, X.; Li, C.; Liu, W.; Wang, K.; Sun, X.; Xu, Y.; Yang, Z.; Cao, Y.; et al. Cationic intermediates assisted self-assembly two-dimensional Ti<sub>3</sub>C<sub>2</sub>T<sub>x</sub>/rGO hybrid nanoflakes for advanced lithium-ion capacitors. *Sci. Bull.* **2021**, *66*, 914–924. [[CrossRef](#)]
40. Liu, C.; Wang, B.; Xu, L.; Zou, K.; Deng, W.; Hou, H.; Zou, G.; Ji, X. Novel Nonstoichiometric Niobium Oxide Anode Material with Rich Oxygen Vacancies for Advanced Lithium-Ion Capacitors. *ACS Appl. Mater. Interfaces* **2023**, *15*, 5387–5398. [[CrossRef](#)]
41. Wang, G.; Wang, F.; Zhang, P.; Zhang, J.; Zhang, T.; Müllen, K.; Feng, X. Polarity-Switchable Symmetric Graphite Batteries with High Energy and High Power Densities. *Adv. Mater.* **2018**, *30*, 1802949. [[CrossRef](#)] [[PubMed](#)]
42. Wrogemann, J.M.; Haneke, L.; Ramireddy, T.; Frerichs, J.E.; Sultana, I.; Chen, Y.I.; Brink, F.; Hansen, M.R.; Winter, M.; Glushenkov, A.M.; et al. Advanced Dual-Ion Batteries with High-Capacity Negative Electrodes Incorporating Black Phosphorus. *Adv. Sci.* **2022**, *9*, 2201116. [[CrossRef](#)]
43. Rothermel, S.; Meister, P.; Schmuelling, G.; Fromm, O.; Meyer, H.-W.W.; Nowak, S.; Winter, M.; Placke, T. Dual-graphite cells based on the reversible intercalation of bis(trifluoromethanesulfonyl)imide anions from an ionic liquid electrolyte. *Energy Environ. Sci.* **2014**, *7*, 3412–3423. [[CrossRef](#)]
44. Read, J.A.; Cresce, A.V.; Ervin, M.H.; Xu, K. Dual-graphite chemistry enabled by a high voltage electrolyte. *Energy Environ. Sci.* **2014**, *7*, 617–620. [[CrossRef](#)]
45. Qiao, Y.; Jiang, K.; Li, X.; Deng, H.; He, Y.; Chang, Z.; Wu, S.; Guo, S.; Zhou, H. A Hybrid Electrolytes Design for Capacity-Equivalent Dual-Graphite Battery with Superior Long-Term Cycle Life. *Adv. Energy Mater.* **2018**, *8*, 1801120. [[CrossRef](#)]
46. Heckmann, A.; Thienenkamp, J.; Belrop, K.; Winter, M.; Brunklaus, G.; Placke, T. Towards high-performance dual-graphite batteries using highly concentrated organic electrolytes. *Electrochim. Acta* **2018**, *260*, 514–525. [[CrossRef](#)]
47. Wang, A.; Yuan, W.; Fan, J.; Li, L. A Dual-graphite Battery with Pure 1-Butyl-1-methylpyrrolidinium bis(trifluoromethylsulfonyl) Imide as the Electrolyte. *Energy Technol.* **2018**, *6*, 2172–2178. [[CrossRef](#)]

48. Huang, Y.; Xiao, R.; Ma, Z.; Zhu, W. Developing Dual-Graphite Batteries with Pure 1-Ethyl-3-methylimidazolium Trifluoromethanesulfonate Ionic Liquid as the Electrolyte. *ChemElectroChem* **2019**, *6*, 4681–4688. [[CrossRef](#)]
49. Ghosh, S.; Sarma, D.; Mahata, A.; Martha, S.K. Differences between cation and anion storage electrochemistry of graphite and its impact on dual graphite battery. *J. Power Sources* **2024**, *589*, 233721. [[CrossRef](#)]
50. Zhang, L.; Wang, H. Dual-Graphite Batteries with Flame-Retardant Electrolyte Solutions. *ChemElectroChem* **2019**, *6*, 4637–4644. [[CrossRef](#)]

**Disclaimer/Publisher’s Note:** The statements, opinions and data contained in all publications are solely those of the individual author(s) and contributor(s) and not of MDPI and/or the editor(s). MDPI and/or the editor(s) disclaim responsibility for any injury to people or property resulting from any ideas, methods, instructions or products referred to in the content.